8

Micropipe Reactions in Bulk SiC Growth

M. Yu. Gutkin,[1,2,3] T. S. Argunova,[4,6] V. G. Kohn,[5]
A. G. Sheinerman[1] and J. H. Je[6]
[1]*Institute of Problems of Mechanical Engineering, RAS, St. Petersburg*
[2]*Department of Physics of Materials Strength and Plasticity, St. Petersburg State Polytechnical University, St. Petersburg*
[3]*Department of Theory of Elasticity, St. Petersburg State University, St. Petersburg*
[4]*Ioffe Physical-Technical Institute, RAS, St. Petersburg*
[5]*National Research Center 'Kurchatov Institute', Moscow*
[6]*X-ray Imaging Center, Department of Materials Science and Engineering, Pohang University of Science and Technology, Pohang*
[1,2,3,4,5]*Russia*
[6]*Republic of Korea*

1. Introduction

Structural defects in silicon carbide (SiC) single crystals such as dislocations, micropipes, inclusions, etc., have been investigated by different methods, including x-ray diffraction topography (Huang et al., 1999), visible light and scanning electron microscopies (SEM) (Epelbaum & Hofmann, 2001; Kamata et al., 2000), AFM and TEM (Yakimova et al., 2005). In particular, defects were imaged in polarized light (Ma, 2006) or made visible in electron beam-induced current and electroluminescence images (Wang et al., 2005). Their morphology has been classified and examined well enough. However, the correlation between structure and morphology still remains an important issue, in which a direct correspondence is complicated by transformation behaviors of structural defects. For example, micropipes — superscrew dislocations with hollow cores (Frank, 1951; Huang et al., 1999) — can dissociate into full-core dislocations (Epelbaum & Hofmann, 2001; Kamata et al., 2000; Yakimova et al., 2005) and react with each other (Gutkin et al., 2009a; Ma, 2006) or with foreign polytype inclusions (Gutkin et al., 2006; Ohtani et al., 2006).

Recent developments have stimulated the progress in defect studies. The push was the production of high-quality crystals (Müller et al., 2006; Nakamura et al., 2004). For example, 4*H*-SiC with micropipe densities as low as 0.7 cm^{-2} is commercially available; and the growth of the epitaxial layers with a dislocation density < 10 cm^{-2} has been demonstrated (Müller et al., 2006). Such low defect densities are very suitable for x-ray imaging techniques, whose development is pulled by the advent of synchrotron radiation (SR) sources. The combination of synchrotron x-ray topography and optical microscopy succeeded in shedding light on the elucidation of the origin and transformation of dislocations and stacking faults (Tsuchida et al., 2007). The highly coherent beams allowed to analyze dislocation types and structures (Nakamura et al., 2007; Wierzchowski et al., 2007), the Burgers vectors senses and

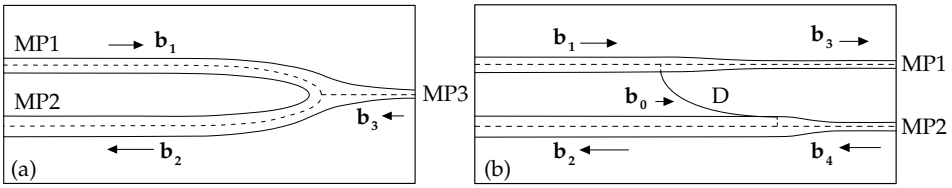

Fig. 1. Sketch of the contact (a) and contact-free (b) reactions between micropipes MP1 and MP2 in a longitudinal section of growing SiC crystal. (a) The micropipes contain superscrew dislocations with opposite Burgers vectors $\mathbf{b}_1$ and $\mathbf{b}_2$. The micropipes meet each other and react, forming a new micropipe MP3 that contains a superscrew dislocation with the sum Burgers vector $\mathbf{b}_3=\mathbf{b}_1+\mathbf{b}_2$. (b) The micropipes contain superscrew dislocations with opposite Burgers vectors $\mathbf{b}_1$ and $\mathbf{b}_2$. Micropipe MP1 emits a half-loop of full-core dislocation D with Burgers vector $\mathbf{b}_0$. As a result, the Burgers vector of MP1 changes from $\mathbf{b}_1$ to $\mathbf{b}_3=\mathbf{b}_1-\mathbf{b}_0$, and the radius of MP1 decreases. Dislocation D glides from MP1 to MP2; the frontal (top) segment of D is absorbed by MP2. Micropipe MP2 changes its Burgers vector from $\mathbf{b}_2$ to $\mathbf{b}_4=\mathbf{b}_2+\mathbf{b}_0$, and, as a consequence, also decreases its radius.

magnitudes (Chen et al., 2008; Nakamura et al., 2008), and the propagation and distribution of threading dislocations (Kamata et al., 2009) in detail .

A decisive advantage of third generation SR sources is the availability of phase contrast imaging which has a strong potential for studying hollow defects in SiC. To image objects with relatively small cross sections, such as micropipes, high temporal coherence is not necessary; and the spatial coherence required is directly yielded by SR source. In this work, we briefly survey the results of white beam phase contrast imaging to investigate the reactions of micropipes in SiC. We also give a short review of their experimental characterization, theoretical modeling, and computer simulation. The improvement of the crystal quality enabled us to develop our research from the collective effects in dense groups of micropipes to remote interactions between distant micropipes. The morphology of individual micropipe, which was not resolvable by diffraction topography, has been examined by phase-contrast imaging. The computer simulation of phase contrast images allowed us to determine the cross-section sizes of micropipes (Kohn et al., 2007).

In our experimental studies, different transformations and reactions between micropipes in SiC crystals have been documented: ramification of a dislocated micropipe into two smaller ones (Gutkin et al., 2002); bundling and merging that led to the generation of new micropipes or annihilation of initial ones (Gutkin et al., 2003a;b); and interaction of micropipes with foreign polytype inclusions (Gutkin et al., 2006) followed by agglomeration and coalescence of micropipes into pores (Gutkin et al., 2009b).

Theoretical analyses of micropipes interactions show that micropipe split happens if the splitting dislocation overcomes the pipe attraction zone and the crystal surface attraction zone; bundling and twisting of dislocation dipoles arise when two micropipes are under strong stress fields from dense groups of other micropipes; micropipes are attracted by foreign polytype inclusion stress fields, initiating the nucleation and growth of pore on the inclusion. When micropipes come in contact with each other [Fig. 1(a)], strong interactions occur. Such interactions are expected to become less probable for low micropipe densities. In the meanwhile, remote elastic interactions between dislocations were detected and known to govern the propagation of elementary screw dislocations (Nakamura et al., 2008). In our study we experimentally measured the variation in cross-sections of two neighboring micropipes and revealed that they reduced their diameters (approximately by half) one after another

	Spectrum	Effective size, μm	Divergence, μrad	Source-sample
Source	6–40 keV	160(H) $\times$ 60(V)	5(H) $\times$ 2(V)	34 m
	Sensitivity	Matrix size, px	View field, (H)	CCD-sample
Detector	14 bit	1600(H) $\times$ 1200(V)	4 mm–280 μm	5 cm–1 m

Table 1. Source and detector attributes for x-ray imaging

during the crystal growth (Gutkin et al., 2008). This 'contact-free' reaction between two micropipes, MP1 and MP2, as illustrated in Fig. 1(b), is different with a 'contact' reaction [Fig. 1(a)]. Here MP1 and MP2 contain opposite-sign superscrew dislocations with Burgers vectors $\mathbf{b}_1$ and $\mathbf{b}_2$, respectively.

In the 'contact' reaction, the elastic attraction of the two opposite dislocations induces the gradual shift of the two micropipes to each other during the crystal growth, resulting in the formation of a new micropipe MP3 containing a new superscrew dislocation with the sum Burgers vector $\mathbf{b}_3 = \mathbf{b}_1 + \mathbf{b}_2$, $b_3 < (b_1, b_2)$, where b_i is the Burgers vector magnitude, $i = 1, 2, 3$. As the micropipe radius is in the quadratic dependence on its Burgers vector magnitude (Frank, 1951), the profit of this reaction is evident: instead of two micropipes we get only one with a much smaller radius. In the special case of $b_3 = b_0$, where b_0 is the Burgers vector magnitude of the elemental full-core dislocation, micropipe MP3 is normally healed.

In case of a contact-free interaction micropipe MP1 emits a full-core dislocation half-loop D, which expands by gliding, reaches the surface of micropipe MP2 and reacts with its dislocation. The corresponding dislocation reactions are described by equations: $\mathbf{b}_1 - \mathbf{b}_0 = \mathbf{b}_3$ and $\mathbf{b}_2 + \mathbf{b}_0 = \mathbf{b}_4$, where $\mathbf{b}_3$ and $\mathbf{b}_4$ are the Burgers vectors of micropipes MP1 and MP2, respectively. This reaction explains the radii reduction of both micropipes by the emission of the full-core dislocation in MP1 and its absorption in MP2. Strong reduction in the radii can lead to their gradual healing.

Reaction between micropipes is always a positive process in view of their elimination during the crystal growth. Therefore, one should better understand the mechanisms of reactions and the factors stimulating such reactions. In our studies, micropipes are assumed to be screw dislocations with hollow cores (Huang et al., 1999), as made certain by combining phase contrast and bragg-diffraction imaging.

2. Samples and techniques

SiC crystals were grown by the sublimation sandwich method. In this technique Si-C vapor species brought from the source (polycrystalline SiC powder) are sublimated on the seed (a crystalline SiC wafer). The source and the seed are separated by a small distance and put into the growth container with an axial temperature gradient. To improve the quality of SiC crystals, a tantalum container was used (Vodakov et al., 1997). The container was filled with Ar (the Ar pressure: 80 mbar). The growth temperature was 2180° C, and the growth rate was 0.5 mm $\times$ h^{-1}. Polytype inclusions were studied by using n-type crystals N-doped, with a donor concentration 2×10^{18} cm^{-3}. They contained B to a concentration (1–2) $\times 10^{17}$ cm^{-3}. Besides, doping of SiC by Al to a concentration of approximately (2–7) $\times 10^{17}$ cm^{-3} occurred because of the presence of Al in the polycrystalline SiC source. The samples were on-axis wafers cut perpendicular to the [0001] growth direction and axial-cut slices along the growth direction obtained from 4*H* and 6*H* boules. The wafers were polished from the both sides down to $\approx$ 0.4 mm thick.

X-ray imaging experiments were performed on the 7B2 X-ray Microscopy beamline at the Pohang Light Source (PLS) in Pohang, Korea. The source was the 7B2 bending magnet port of the PLS storage ring. Unmonochromatized ('white') beam was propagated through polished beryllium window of 2 mm thick and then through a specimen with no optical elements in between. Passing through a $CdWO_4$ scintillator crystal of 200 μm thick, the X-ray beam was converted to visible lights, which were then reflected from a mirror (a polished silicon wafer) and directed to a detector with a charge coupled device (CCD) matrix. The source and the detector attributes are listed in table 1. Prior to recording, the visible light image was magnified by a lens system with the magnification $1\times-50\times$. Under a low magnification [for example, by using 1500 μm (H) view field] the overall defect density and distribution were visualized. The $\approx$300 μm (H) view field provided a very useful enlargement for the examination of micropipes. Optical micrographs were taken on a Zeiss universal microscope equipped with a CCD. Scanning electron microscopy was done on a JEOL JSM-6330F FESEM operating at 12 kV. Photoluminescence (PL) images of polytype inclusions were taken with the PL microscope in visible as well as ultraviolet lights under the magnifications of $50\times-200\times$.

3. Contact-free reactions between micropipes

3.1 Model

Let us turn back to Fig. 1(b) sketching the contact-free reaction between two micropipes. Direct experimental justifications of this mechanism has not been provided up to now. However, using computer simulation of phase contrast images (Kohn et al., 2007), we have demonstrated the correlated reduction in the radii of two remote micropipes in SiC (Gutkin et al., 2008). As shown below, this effect indirectly supports our model.

The first stage of the contact-free reaction is the split of a dislocation from a micropipe at the crystal growth front. Recently the possibility of such a split event has been analyzed within a three-dimensional model (Gutkin & Sheinerman, 2004). Here we consider a simplified two-dimensional model of a contact-free reaction between two parallel micropipes. Fig. 2 shows micropipes with circular cross sections of the radii r_1 and r_2 that contain screw dislocations with the Burgers vectors $\mathbf{b}_1$ and $\mathbf{b}_2$, respectively. The distance between the micropipe axes is denoted as d. Let the first micropipe emits a screw full-core dislocation with the Burgers vector $\mathbf{b}_0$ [Fig. 2(a)]. We also assume that a shear stress $\tau^0 = \tau^0_{yz}$ associated with thermal stresses appearing during the growth of SiC acts in the region between the examined micropipes and far from their surfaces. To analyze the possibility of the emission, we can use the corresponding variation ΔW on the total energy of the system. It is calculated (per unit dislocation length) using the previous results (Gutkin & Sheinerman, 2002; Gutkin et al., 2009c) for the stresses and energies of dislocations lying in an isotropic medium with two cylindrical voids. However, in the case of interest, when $d \gg r_1, r_2$, it is sufficient to separately consider the effects of the two voids on the shear stress as well as on the image force exerted by the micropipe surfaces on the emitted dislocation and the forces of dislocation interaction. In this approximation, the thermal shear stress τ_{yz} acting on the emitted dislocation in between the micropipes, taken with account for the stress concentration near their surfaces, is $\tau_{yz} = \tau^0[1 + r_1^2/x^2 + r_2^2/(d-x)^2]$, where x is the coordinate of the emitted dislocation. The second and third terms in brackets reflect the effects of the first and second void (Thölén, 1970), respectively, in the limiting case $d \gg r_1, r_2$ when the mutual influence of the voids is negligible. The total elastic force acting on the emitted dislocation (per its unit length) follows

as

$$F\left(d \gg r_1, r_2\right) \approx b_0 \tau_{yz} \tag{1}$$
$$+\frac{G b_0}{2\pi}\left\{\frac{b_1 - b_0}{x} - \frac{b_2}{d-x} + \frac{b_0}{x} - \frac{b_0 x}{x^2 - r_1^2} - \frac{b_0}{d-x} + \frac{b_0 (d-x)}{(d-x)^2 - r_2^2}\right\},$$

where G is the shear modulus. In brackets of formula (1), the first and second terms correspond to the interactions of the emitted dislocation with dislocations within micropipes MP1 and MP2, respectively; the third-fourth and fifth-sixth terms correspond to the image force (Gutkin & Sheinerman, 2002; Pirouz, 1998) exerted by the surface of MP1 and MP2, respectively.

The energy ΔW associated with dislocation emission is given by $\Delta W = \int_{r_1}^{x-b_0} F(x)dx + W_c$, where $W_c \approx G b_0^2/(4\pi)$ is the dislocation core energy (Hirth & Lothe, 1982). Substitution of (1) to the latter relation for ΔW yields:

$$\Delta W = b_0 \tau^0 \left(x - \frac{r_1^2}{x} + \frac{r_2^2}{d-x} - \frac{r_2^2}{d-r_1}\right) \tag{2}$$
$$+\frac{G b_0^2}{4\pi}\left\{1 + \ln\frac{\left(x^2 - r_1^2\right)\left[(d-x)^2 - r_2^2\right]}{b_0 r_1 (d-x)^2} + \frac{2b_1}{b_0}\ln\frac{r_1}{x} + \frac{2b_2}{b_0}\ln\frac{d}{d-x}\right\}.$$

In the following calculations, we will use the Frank relation (Frank, 1951) $r_i = G b_i^2/(8\pi^2\gamma)$ between the Burgers vectors magnitudes b_i and micropipe radii r_i, where γ is the surface energy. Numerical evaluation of ΔW for the case of growing 4*H*-SiC crystal with $G = 165$ GPa, $\gamma/G = 1.4 \cdot 10^{-3}$ nm (Si et al., 1997) and equilibrium micropipes [for which the Frank relation (Frank, 1951) is valid] shows that ΔW depends primarily on the Burgers vectors of micropipe dislocations and on the level of thermal shear stress τ_0 [Fig. 2(b,c)].

Let us first consider the case when $\tau^0 = 0$ [Fig. 2(b)]. As is seen, the dislocation exchange is most energetically favorable if the Burgers vectors $\mathbf{b}_1$ and $\mathbf{b}_2$ are opposite in sign. At the same time, to move from one micropipe to the other, the emitted dislocation must overcome an energetic barrier. If the Burgers vectors of the two micropipes are of the same sign, the emitted dislocation must overcome two energetic barriers on its way from one micropipe to the other. In this case, the possibility for the dislocation exchange between these micropipes is governed by the difference of the Burgers vector magnitudes. If $(b_1 - b_2) < 3b_0$, then we have: $\Delta W > 0$, and the dislocation exchange is impossible. If $(b_1 - b_2 \geq 3b_0)$, then the dislocation reaction can occur if the emitted dislocation is able to overcome the two energetic barriers. The presence of two energetic barriers results in the appearance of an equilibrium position for the emitted dislocation, situated in between the micropipes.

Figure 2(c) shows the case where micropipes initially have the same Burgers vectors, equal in magnitude to $7b_0$, and the dislocation emission occurs under the action of a thermal shear stress τ^0. One can see that the stress τ^0 reduces the energetic barriers for the dislocation exchange. In the range of stress values from 10 to 100 MPa, which are characteristic for bulk SiC growth (Ma et al., 2003; Müller et al., 2000), the first barrier decreases weakly while the second one strongly. The first barrier has the height of about $1.5 G b_0^2/\pi$ per unit dislocation length, which for a 4*H*-SiC crystal with $G = 165$ GPa and $b_0 = 1$ nm gives $\approx 0.48 G b_0^2 l \approx$ 125 eV per unit distance $l \approx 0.252$ nm (Dudley et al., 2003) between basal atomic planes. This value is obviously very high that is not surprising due to the model of an infinite medium considered within the classical theory of linear elasticity. Moreover, in reality, the dislocation

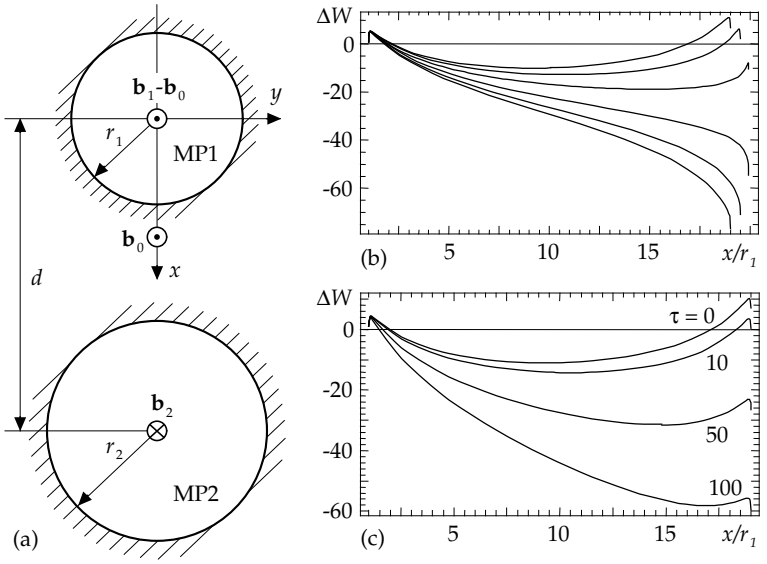

Fig. 2. A model of contact-free reaction between two micropipes realized through screw dislocation exchange. Micropipe MP1 emits a dislocation with the Burgers vector $\mathbf{b}_0$, which moves to micropipe MP2 and is absorbed by it (a). Dependences of the energy ΔW associated with the emission of a dislocation by a micropipe near a second micropipe on the normalized dislocation coordinate x/r_1 for $d/r_1 = 20$ and $b_1/b_0 = 7$. (b) $\tau^0 = 0$ and $b_2/b_0 = -7, -5, -2$, 2, 5, 7 (from bottom to top). (c) $b_2/b_0 = 7$ and $\tau^0 = 0$, 10, 50, and 100 MPa. The energy ΔW is given in units of $Gb_0^2/4\pi$, the stress values are given at the curves in MPa.

emission is expected to occur within a rather thin subsurface layer under the growth front where the conditions can be very far from equilibrium due to high temperature and surface effects. The height of the second barrier is approximately five times higher at $\tau^0 = 0$ but it falls down to $\approx 0.16Gb_0^2l$ at $\tau^0 = 100$ MPa. The equilibrium position of the emitted dislocation increases from $\approx 9r_1$ at $\tau^0 = 0$ to $\approx 17r_1$ at $\tau^0 = 100$ MPa. One can conclude that thermal shear stress greatly promotes dislocation transfer and makes it possible even in the case of micropipes having large Burgers vectors of the same sign.

3.2 Correlated reduction in micropipe cross sections in SiC growth

To observe micropipe cross-sections at different distances from the surface of a grown crystal, we prepared a special sample, which was axial-cut slice along the growth direction (0001) obtained from 4*H*-SiC boule. So micropipes located almost parallel to the growth axis were nearly parallel to the surface. Micropipes grouped along the boundaries of foreign polytype inclusions (6*H* and 12*R*) which appeared at ≈1 cm distance from the seed/boule interface. Below the inclusions over the area of 1 cm^2 micropipes were undetectable. The sample (rotated to have a horizontal position of the micropipe axis for better edge enhancement in a more coherent vertical direction) was sequentially placed at different distances from the detector. We obtained nine images for the distances from 5 to 45 cm starting with the first image registered at 5 cm from the sample. Three micropipes forming a group were examined: two in contact and the third lying remotely. The variation in cross-section sizes along the axes of MP1 and MP2 from the group are shown in Fig. 3(a), while phase contrast image of the

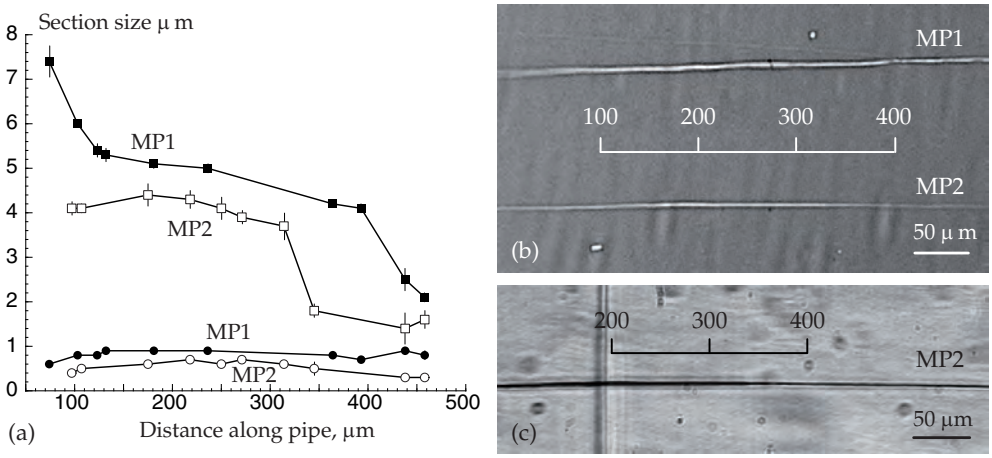

Fig. 3. (a) Variation in cross-section sizes along the axes of MP1 and MP2 from the group of micropipes (squares – transverse and circles – longitudinal diameters, respectively); (b) phase contrast image of the group (the growth direction is from left to right); (c) optical micrograph in transmission light of MP2 lying remotely from two micropipes in contact.

group and the optical micrograph of the remote micropipe MP2 are demonstrated in (b) and (c), respectively.

For all sample-to-detector distances and for different points along the axis of micropipes, the intensity profiles normal to the axis were measured. To determine the characteristic sizes of the micropipe cross sections in different points along the micropipe axis, we applied a computer simulation (Kohn et al., 2007) of the measured intensity profiles, assuming that these sections can have variations in longitudinal (along the beam) and transverse (across the beam) sizes. For every micropipe cross section under investigation, the computer program calculated many profiles for various possible section sizes on the base of Kirchhoff propagation (Kohn et al., 2007) to find the profile, which gives the best fit to the experimental profile registered for this section. The coincidence allowed us to determine both the longitudinal and transverse sizes of the section. We found that the micropipes had elliptical cross sections extended in transverse direction. The transverse and longitudinal diameters of micropipes MP1 and MP2 are presented in Fig. 3(a) versus the distance along the pipe axes increasing in the growth direction. It is seen that, with growth, the transverse size of MP1 reduces from 7.4 to 2.1 μm. At the same time, the transverse size of the MP2 reduces from 4.1 to 1.6 μm. In contrast, the longitudinal diameters remain almost the same and of the order of 0.8 μm for the MP1 and 0.5 μm for the MP2. In the correlated decrease of MP1 and MP2 cross section sizes in Fig. 3(b) several features are apparent. A remarkable decrease of the MP1 cross section size occurs in the distance interval from 74 to 132 μm while the transverse diameter of MP2 drastically decreases later in the distance interval from 314 to 345 μm. In addition, a rapid decrease of the transverse diameter of MP1 happens in the distance interval from 393 to 458 μm when the transverse diameter of MP2 remains almost invariable.

We explain the changes in the cross sections of the two neighboring micropipes by the contact-free reaction between them. Experimental data in Fig. 3(a, b) tend to confirm the reaction schematically shown in Fig. 1(b). Most likely, during the rapid decrease of its cross section area MP1 emits a full-core dislocation moving towards MP2 and finally absorbed by it.

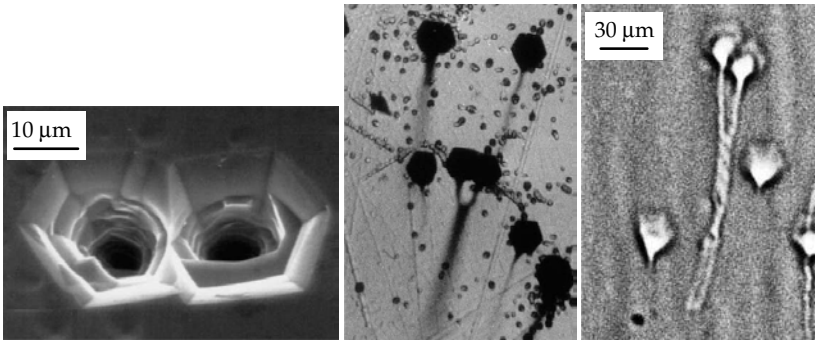

(a) SEM (b) Optics (c) X-rays

Fig. 4. (a) SEM image of a ramified micropipe; (b) transmission light microscopy image of the same micropipe; (c) SR phase-contrast image of another ramified configuration.

For a new possible mechanism of the contact-free reactions between micropipes, our calculations have demonstrated that, depending on the signs of the micropipe Burgers vectors (prior to dislocation exchange between micropipes), the moving dislocation must overcome one or two energetic barriers. In the case where the initial micropipe Burgers vectors are of the same sign, the dislocation exchange can happen only if the difference between the micropipe Burgers vector magnitudes is large enough (not less than three magnitudes of the elementary Burgers vector). The energetic barrier(s) that the dislocation has to surmount on its way from one micropipe to the other can supposedly be overcome under the growth front where the conditions can be very far from equilibrium due to high temperature and surface effects. Correlated reduction in micropipe cross-sections indirectly supports our suggestion that micropipes can interact each other without a direct contact, by the proposed mechanism.

4. Elastic interaction and split of micropipes

4.1 Ramification of micropipes

Three imaging techniques: SEM, optical microscopy, and x-ray phase contrast imaging were applied to study the split of micropipes. The SiC samples were on-axis wafers cut perpendicular to the [0001] growth direction, and the ends of screw dislocations with Burgers vector aligned along the [0001] axis were visible on the etched (0001) surface. A typical SEM image of a ramified dislocation with a hollow core is shown in Fig. 4(a), and Fig. 4(b) is a transmission light image of the same configuration. However, SEM is insensitive and light microscopy is limitedly suited for the detection of micropipes in the wafer interior. By using the phase contrast imaging [Fig. 4(c)] ramified micropipes were clearly detected in the bulk, and the numbers of single and ramified ones within each view field were calculated. It appeared that the density of nearby single dislocations as well as the presence of dislocation boundaries did not influence the number of ramified micropipes. Their distribution over the wafer area was almost homogeneous with an average density of two per each view field, the latter being 0.6×0.4 mm^2.

Let us determine when a dislocated micropipe is favorable to split into a pair of parallel micropipes with smaller radii and Burgers vectors. For the sake of simplicity, we focus on the case when the angle between ramifying segments of the micropipe "tree" is small enough to allow one to model these segments as a pair of parallel micropipes extending through the entire crystal.

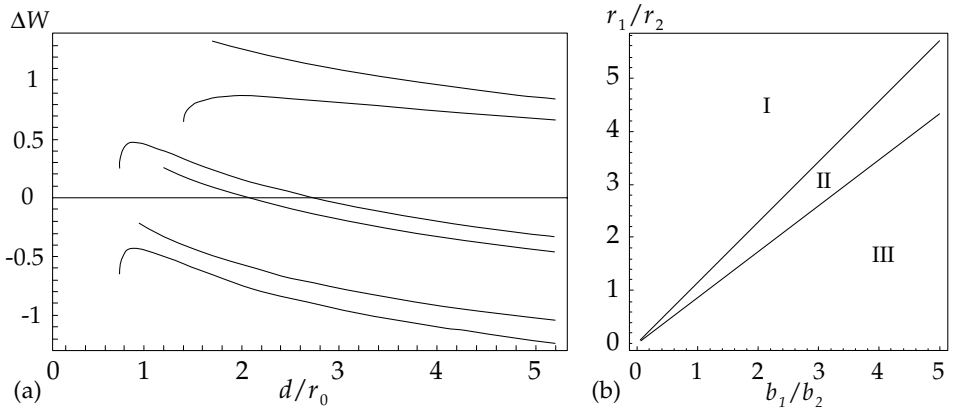

Fig. 5. (a) The dependences of ΔW [in units of $Gb_0^2/(4\pi)$] on the normalized distance d/r_0 between the micropipe axes, for the following values of parameters: ($\widetilde{r}_1 = 0.05$, $\widetilde{r}_2 = \widetilde{b}_1 = 0.5$, $\kappa = 3$), ($\widetilde{r}_1 = 0.3$, $\widetilde{r}_2 = 0.45$, $\widetilde{b}_1 = 0.4$, $\kappa = 3$), ($\widetilde{r}_1 = \widetilde{r}_2 = \widetilde{b}_1 = 0.5$, κ=1), ($\widetilde{r}_1 = 0.05$, $\widetilde{r}_2 = \widetilde{b}_1 = 0.5$, $\kappa = 1$), ($\widetilde{r}_1 = 0.3$, $\widetilde{r}_2 = \widetilde{b}_1 = 0.8$, $\kappa = 3$), and ($\widetilde{r}_1 = 0.6$, $\widetilde{r}_2 = 0.9$, $\widetilde{b}_1 = 0.4$, $\kappa = 3$), from bottom to top. (b) The system state diagram in the coordinate space (b_1/b_2, r_1/r_2). The curves separate parameter regions I and III, where both attraction area and unstable equilibrium position exist for two micropipes, from parameter region II, where the micropipes repulse at any distance.

The crystal is modeled as an isotropic medium with the shear modulus G and specific surface energy γ. Let the radius and the Burgers vector of the micropipe prior to the split be r_0 and $\mathbf{b}_0 = b_0\mathbf{e}_z$ while the radii and the Burgers vectors of two micropipes generated due to the split be r_1, r_2 and $\mathbf{b}_1 = b_1\mathbf{e}_z$, $\mathbf{b}_2 = b_2\mathbf{e}_z$, respectively. The distance between the micropipe axes is denoted by d while that between the micropipe free surfaces is designated by h (h=d - r_1 - r_2). We suppose that the micropipe ramification is possible if the energy of two growing ramifying micropipe segments (per their unit length) is smaller than the energy of the original micropipe (per its unit length). Also, we assume that the micropipe ramification requires the repulsion of the ramifying segments. To find the conditions for the split we have calculated the energy change due to the split of a micropipe into two contacting ones and the interaction force between two parallel micropipes (Gutkin et al., 2002).The energy ΔW resulting from the micropipe split is shown in Fig. 5(a). It is presented in units of $Gb_0^2/(4\pi)$ in dependence on the normalized distance d/r_0 between the micropipe axes for different values of the parameters $\widetilde{r}_1 = r_1/r_0$, $\widetilde{r}_2 = r_2/r_0$, $\widetilde{b}_1 = b_1/b_0$, and $\kappa = 8\pi^2\gamma r_0/(Gb_0^2)$. As is seen in Fig. 5(a), ΔW either monotonously decreases with d or has a maximum. In the first case, the micropipes formed due to the split repulse at any distance. If the curve ΔW has a maximum, the micropipes repulse at any distance greater than some critical distance d_c and attract each other at distances smaller than d_c. In this case, the micropipes separation requires overcoming an energetic barrier.

It is important to note that the reverse process of the micropipe merging may follow the micropipe split. Indeed, the split may be possible only on account of the reduction in the total micropipe surface area. If the micropipes formed due to the split stay in contact, they are energetically favored to coalesce and produce a single micropipe with a radius close enough to the equilibrium one. In this case, the split and following coalescence of the micropipes results only in a decrease in the micropipe radius, that is, in its partial overgrowth. We suppose that the merging of the micropipe segments generated after the split does not occur if these

segments repulse as soon as they have been formed. As is shown above [see Fig. 5(a)], the micropipes may either repulse at any distance or repulse at distances d greater than the critical distance d_c and attract each other at $d < d_c$. The ramification of the micropipe segments (not followed by their coalescence) is possible if they repulse at any distance or the critical distance d_c [and the corresponding energy barrier $W(d = d_c) - W(d = r_1 + r_2 + a)$ that the micropipes have to overcome to go outside of the attraction area] is small enough.

Now let us determine the parameter region where the ramifying micropipe segments (modeled as a pair of parallel micropipes) repulse at any distance. This parameter region is shown in Fig. 5(b) that depicts the system state diagram in the coordinate space $(b_1/b_2, r_1/r_2)$. The upper and lower curves separate regions I and III, where the micropipes attract each other at short distances while they repel each other at long distances, and the corresponding critical distance $h_c = d_c - r_1 - r_2$ between the micropipe free surfaces exists, from region II, where the micropipes repulse at any distance. As is seen, an attraction area may exist for two same-sign micropipes if b_1/b_2 and r_1/r_2 differ by more than 15%–25%.

The parameter region where the micropipe ramification does not require overcoming an energetic barrier is given by the intersection of the corresponding parameter regions shown in Fig. 5(a, b). Such a ramification is possible if the micropipes are of the same sign, the radius of the original micropipe exceeds the equilibrium one, the total micropipe surface area reduces due to the ramification, and the radii of the ramifying micropipes are approximately in the same ratio as the magnitudes of their dislocation Burgers vectors.

4.2 Merging and twisting of micropipes

Many morphologies of twisted and coalesced micropipes have been observed experimentally in SiC crystals by means of x-ray phase contrast imaging. The examples of twisted configurations are shown in Figs. 6(a) and 7(a). To explain these phenomena, we have

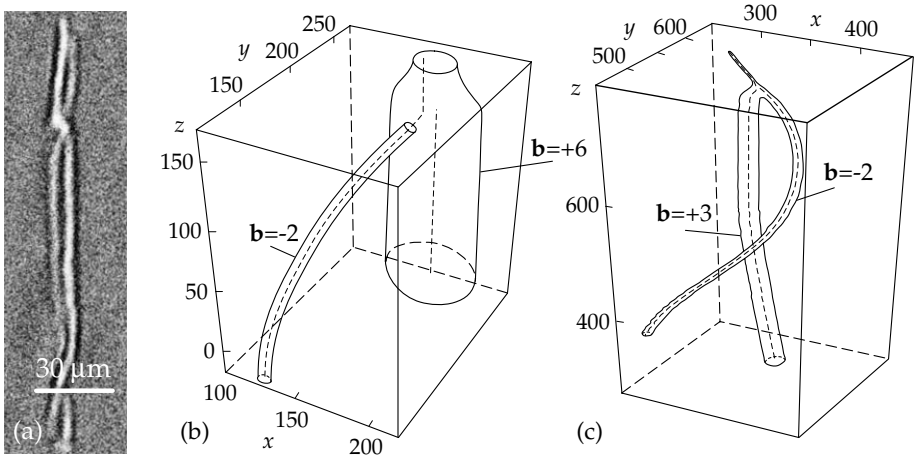

Fig. 6. SR phase-contrast image of micropipe twisting (a); coalescence of micropipes with different magnitudes of Burgers vectors results in the generation of a new micropipe segment (b, c). The coalescing micropipes come to each other along the shortest way (b) or twist (c). The Burgers vectors are shown in units of c, which is the lattice parameter in the growth direction. The coordinates x and y are given in units of $Gc^2/(8\pi^2\gamma)$. The length of micropipes (along the z axes) is in arbitrary units that depend on the growth rate.

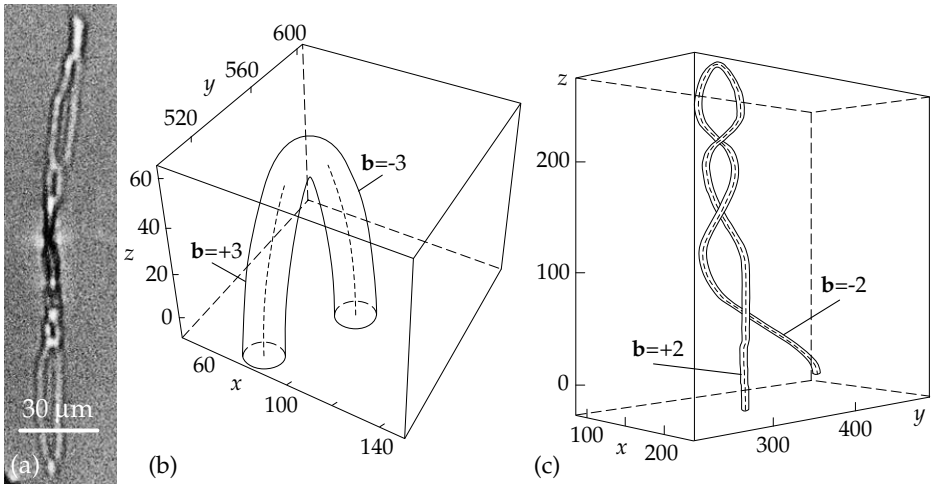

Fig. 7. SR phase-contrast image of semi-loops resulting from macropipes twisting (a); coalescence of micropipes with equal magnitudes of Burgers vectors results in the annihilation of the subsurface micropipe segments (b, c). The coalescing micropipes come to each other along the shortest way (b) or twist (c). For the units see the caption to Fig. 6.

performed a computer simulation of micropipe evolution (Gutkin et al., 2003a;b). For computer modeling, a simple computer code has been elaborated to simulate 2D dynamics of pipes within Newton's approach. We considered the lateral motion of subsurface micropipe segments. The equations of the motion of subsurface micropipe segments had the form:

$$m_k \mathbf{a}_k = \frac{G b_k}{2\pi} \sum_{i \neq k} b_i \left(\sqrt{h^2 / r_{ik}^2 + 1} - 1 \right) \mathbf{e}_{ik} - 4\gamma R_k \mathbf{e}_k, \tag{3}$$

where k denotes the number of a specified micropipes, i denotes the numbers of other micropipes, $\mathbf{a}_k$ is the micropipe segment acceleration, m_k is its effective mass, R_k is its radius, G is the shear modulus, b_k is the projection of the micropipe dislocation Burgers vector onto the direction of the dislocation line, h is the height of subsurface micropipe segments, γ is the specific surface energy, r_{ik} is the distance between the ith and kth micropipes, $\mathbf{e}_{ik}$ is the unit vector directed from the ith to the kth micropipe, and $\mathbf{e}_k$ is the unit vector whose direction coincides with the direction of the lateral micropipe motion. The first term on the right-hand side of formula (3) describes the total force of the interaction of the k-th micropipe with other micropipes, while the second term specifies the force of surface tension related to the steps appearing on micropipe cylindrical surfaces during lateral displacements of micropipe segments.

As a result of the simulation, various reactions between the subsurface micropipe segments were observed. It has been shown that the reaction of micropipe coalescence gives rise to the generation of new micropipes with smaller diameters and Burgers vectors or annihilation of initial micropipes (see Figs. 6,7), which leads to diminishing their average density. Using the results of 2D simulation, we reconstructed some typical defect configurations in a 3D space. They may be subdivided into planar and twisted micropipe configurations. The planar configurations arise when the interacting pair of micropipes has incomparable diameters or is located far (at the distance of more than about 5 average micropipe diameters) from other

micropipes. The twisted configurations like double spirals form if the interacting micropipes have comparable diameters and are located within dense groups of other micropipes.

5. Role of micropipes in the formation of pores at foreign polytype boundaries

5.1 Interaction of micropipes with polytype inclusions

SR phase contrast imaging, optical and scanning electron microscopies, and color photoluminescence have been used to study the interaction of micropipes with foreign polytype inclusions in 4*H*-SiC bulk crystals. The boules had been grown on carbon-terminated faces of the 6*H*-SiC seeds by the sublimation sandwich method in Ar atmosphere and in the presence of Sn vapor. The Sn vapor promotes the transformation of the polytype of the substrate into 4*H*-SiC (Vodakov et al., 1997). Several wafers were cut from 4*H*-SiC boules. One wafer, 0.4 mm thick and misoriented 8° away from the basal plane, was further cut into 0.5 mm wide bars. X-ray experiment was performed in two regimes: (1) via the translation of the wafer to map micropipe distributions over the area and (2) via the rotation of the bar samples to reveal the spatial orientations of macro- and micropores. In the latter case, the rotation axis was perpendicular to the beam and parallel to the long edges of the bar. The rotation interval was 180° with a 2° step. The images were recorded in a step by step sequence.

Figure 8(a) shows SEM image of a typical pore located at the boundary of a foreign polytype inclusion. The pore uncovers a slit on a molten KOH treated surface. Figure 8(b) displays the illumination of the inclusion itself excited by an ultraviolet light at room temperature. When the inclusion is located close to the wafer surface, its polytype can be easily identified by the color of PL. In low N doped samples at room temperature, 6*H* polytype inclusions have yellow PLs (Saparin et al., 1997). A sketch of the inclusion, pore, and micropipes is shown in Fig. 8(c).

For the purposes of the model, it is important to find a way by which micropipes accumulate at the inclusions. Figure 9 shows several representative phase-contrast images registered while rotating the sample in the SR beam. The sample had the shape of a bar. In the image, a relatively thick micropipe [indicated as MP1 on Fig. 9(b)] follows the growth direction, while the much thinner (and therefore much more mobile) MP2 inclines towards the inclusion boundary. On the other hand, the thick MP3 also bends towards the inclusion, and its surface becomes steplike. MP4 revolves about MP5, which follows the growth direction. The inset in (c) displays twisted micropipes turning to another inclusion of 6*H*-SiC in the same crystal.

Earlier, the reactions of micropipes — twisting and bundling — were discussed in terms of the stress fields from the other surrounding micropipes. (Gutkin et al., 2003a;b). However, in this study, stress fields seem to result from the inclusions. The remarkable deviation from the growth direction, the transformation of shape, and the reactions of micropipes prove that they are strongly influenced by the inclusions. Attracted by the inclusions, micropipes collect into

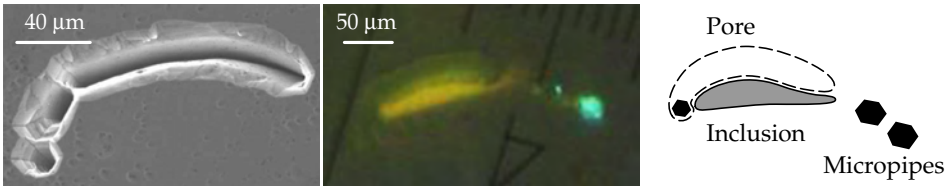

(a) SEM (b) PhL (c) Sketch

Fig. 8. (a) SEM image of the pore. (b) PL image of the inclusion. (c) Sketch of the inclusion, the pore, and the micropipes.

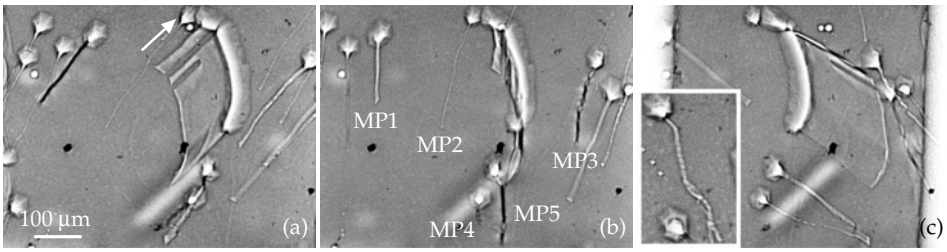

Fig. 9. Representative phase contrast images among the sequences of the images registered while rotating the sample, (a)–(c) show the same region as Fig. 8, the inset in (c) displays the image of twisted micropipe recorded at another place in the same sample, and the growth direction is indicated in (a) by an arrow. The elongated white spot is a defect of the scintillator.

bundles at the inclusion boundaries. This phenomenon was observed throughout this crystal and other similar crystals. The gathering of micropipes is followed by the reduction of their density in the neighboring regions.

The observations were interpreted based on the following model (Gutkin et al., 2006). At the boundaries of the other polytypes inclusions the lattice mismatch should exist that gives rise to essential elastic deformation, whose orientational constituent relaxes with the formation of micropipes. At the sites of micropipe accumulation, micropipes elastically interact, which leads to the merge of several micropipes with the generation of cavities along the inclusion boundaries. As a result, the misfit stresses completely relax. Due to the action of image forces, the free surfaces of the cavities thus formed attract new micropipes and, absorbing them, propagate along the inclusion boundaries.

5.2 Pore growth by micropipe absorption at foreign polytype boundaries

In the previous section we outlined the results of the elastic interaction of micropipes with polytype inclusions. In this section the processes of micropipe accumulation and their coalescence into a pore is discussed. The pores generated in this way may grow at the expense of absorbed micropipes.

We have observed that pores of different sizes and shapes are always present at the boundaries of foreign polytype inclusions in SiC samples under study. Figure 10 illustrates the representative morphology of a typical pore in a 4*H*-SiC wafer. Comparison of the phase-contrast image [Fig. 10(a)] with the PL image [Fig. 10(b)] clearly shows that pores are located along the inclusion boundaries as sketched in Fig. 10(c). The slit pore (1) surrounds one of the inclusion edges, while tubular pores (2)–(5) are located at the inclusion corners. Pore shape reflects a stage in its development. The pore nucleation is initiated as a tube form by initial accumulation of some micropipes near the inclusion boundary. In the process of sequential attraction and absorption of new micropipes, the pore shape changes and step by step transforms into a slit, which can then propagate along the inclusion boundary.

Images of another wafer cut of the same 4*H*-SiC boule are shown in Fig. 11. The SEM image [(Fig. 11(a)] represents etch pits of not only pores, but also micropipes, which appear as faceted pits on the top of the tubes. We see that pores are produced by agglomeration of micropipes. The PL dark green image displayed in the inset to (a) represents a 21*R*-SiC inclusion in the 4*H*-SiC wafer. [At room temperature, n-type 6*H* and 4*H* polytypes containing N and B show yellow and light green PL, respectively, while Al activated luminescence for rombohedral 21*R* polytype taken at 77 K is dark green (Saparin et al., 1997).] The marked pores are located at

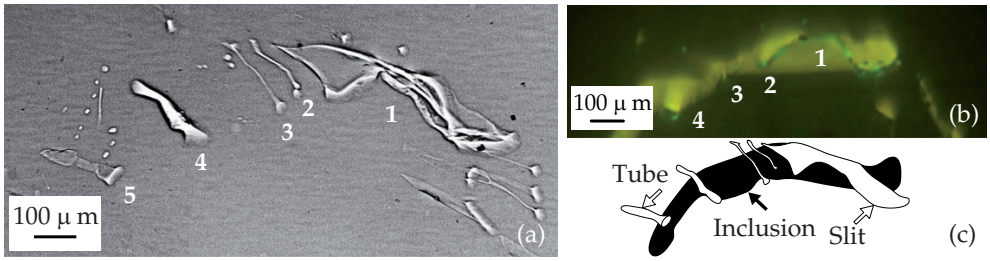

Fig. 10. Pores and micropipes at the boundary of 6*H*-SiC inclusion in 4*H*-SiC wafer. (a) SR phase-contrast image. (b) PL image. (c) The sketch outlines the inclusion and the pores as indicated by the black and white arrows, respectively. The number 1 points to a slit pore and the numbers 2–5 to tubular pores.

the edge of the left (concave) inclusion as defined in Fig. 11(c). The pores spread over the inclusion boundary and propagate deeply inside the wafer. The phase-contrast image [Fig. 4(b)] also reveals that the pores are produced through the coalescence of micropipes. The observed micropipes remarkably deviate from the growth direction, which we attribute to the interaction of micropipes with the polytype inclusion.

Mapping with a lower magnification revealed a significant reduction in micropipe density nearby to the pores, which can be explained by the absorption of micropipes by the pores.

The following scenario for pore growth is suggested, as is illustrated by the sketch in Fig. 12. At the beginning, a few neighboring micropipes are attracted to an inclusion with no pore to accommodate the orientation mismatch between the inclusion and the matrix crystalline lattices [Fig. 12(a)] (Gutkin et al., 2006; 2009b). This orientation mismatch is described mathematically through the components of the inclusion plastic distortions (Gutkin et al., 2006). In the case of two nonvanishing plastic distortion components, micropipes are attracted to a corner of the inclusion [Figs. 12(a) and 12(b)], where they have an equilibrium position (Gutkin et al., 2006; 2009b). Let the first micropipe occupy its equilibrium position at this corner [Fig. 12(b)]. Then another micropipe, containing a dislocation of the same sign as the first micropipe, is attracted by the inclusion to the same equilibrium position. If the inclusion is "powerful" enough (that is the plastic distortions are large), the attraction force exerted by

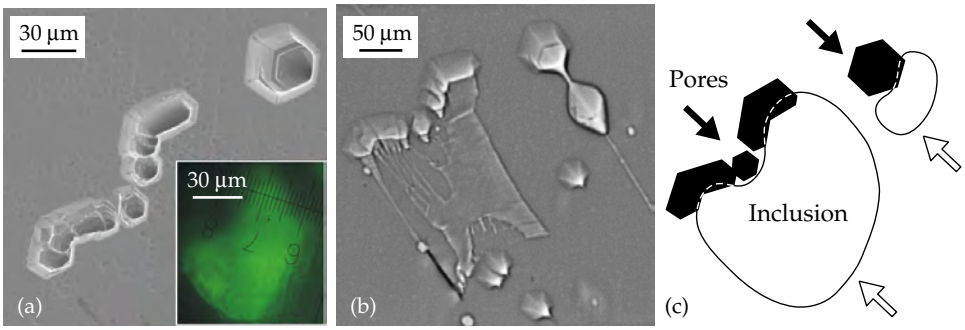

Fig. 11. Agglomeration of micropipes into the pores at the boundary of a 21*R*-SiC inclusion in the 4*H*-SiC wafer. (a) SEM image of the pore. Inset shows PL image of the 21*R*-SiC inclusion. (b) SR phase-contrast image reveals merging of micropipes into slit pores in the wafer interior. (c) Sketch of the inclusion and the pores.

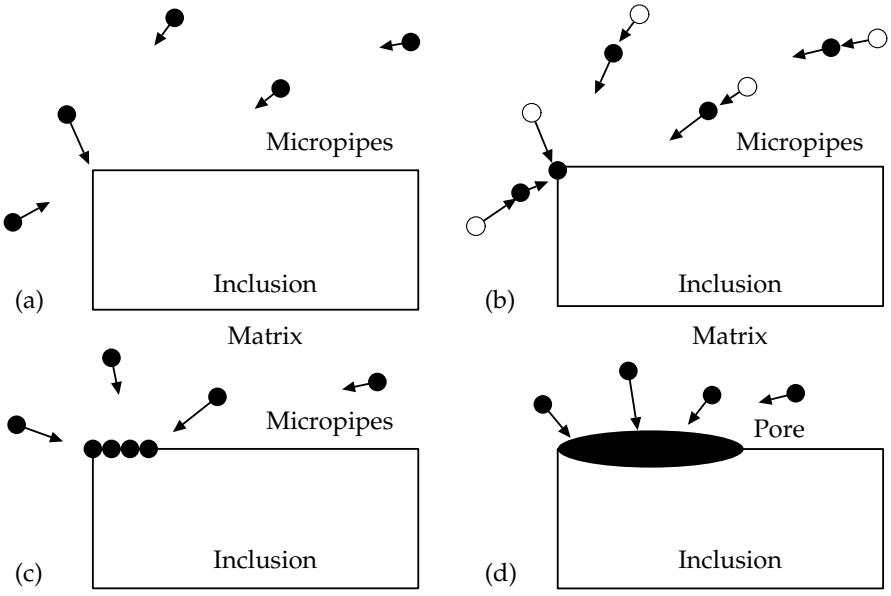

Fig. 12. Scheme of nucleation and extension of a pore at the inclusion/matrix interface through agglomeration of micropipes. (a) Micropipes are attracted to their equilibrium positions at a corner of the inclusion. (b) The first micropipe occupies its equilibrium position at the corner; the others come closer to it. (c) Some micropipes are agglomerated at the corner and form a pore; the others are attracted both to the corner and to the free surface of the pore. (d) The pore propagates along the inclusion/matrix interface by absorption of close micropipes.

the inclusion and the free surface of the first micropipe is stronger than the repulsion force between micropipe dislocations, and so the second micropipe merges with the first one. Some of such micropipes, which have been attracted to this corner [Fig. 12(c)], agglomerate and form a pore. After the pore has been formed, some other micropipes move to the same equilibrium position at the inclusion boundary and are absorbed by the pore [Fig. 12(d)], resulting in the pore growth and the change of the dislocation charge accumulated at the boundary. This process continues until the pore occupies the entire inclusion facet or until the pore size becomes so large that the inclusion stops to attract new micropipes.

To analyze the conditions at which pore growth along a foreign polytype inclusion at the expense of micropipes absorbed is favored, we suggest a two-dimensional (2D) model of the inclusion, pore and micropipes. Within the model, the inclusion is infinitely long and has a rectangular cross-section (Fig. 13). The long inclusion axis (z-axis) is oriented along the crystal growth direction while the inclusion cross-section occupies the region ($x_1 < x < x_2$, $y_1 < y < 0$). The mismatch of the matrix and the inclusion crystal lattices is characterized by the inclusion plastic distortions β_{xz} and β_{yz} (Gutkin et al., 2006). The inclusion/matrix interface contains an elliptic pore, and mobile micropipes lie nearby. The pore is assumed to grow at the expense of micropipes absorbed (Fig. 12). For definiteness, we suppose that the pore is symmetric with respect to the upper inclusion facet y=0. The pore semiaxes are denoted as p and q, and the pore surface is defined by the equation $x^2/p^2 + y^2/q^2 = 1$.

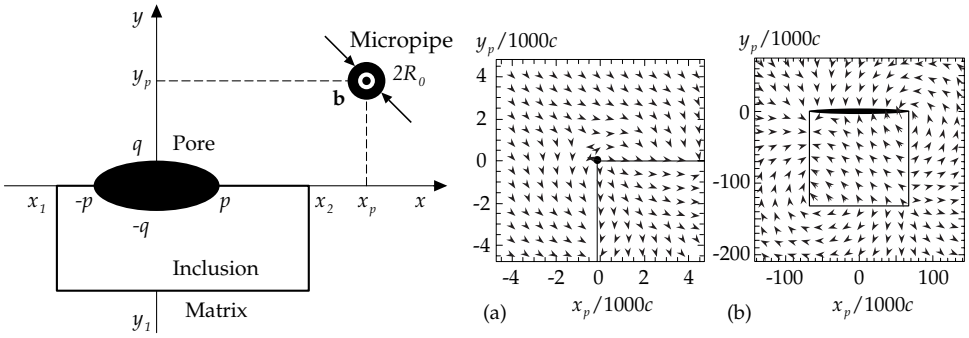

Fig. 13. Elliptic pore at the inclusion boundary and a mobile micropipe nearby.

Fig. 14. Vector fields of the force **F** exerted by a 4*H*-SiC inclusion (containing a pore on its boundary) in a 6*H*-SiC matrix on a mobile micropipe with the magnitude 4*c* of the dislocation Burgers vector. (a) The inclusion plastic distortion components are equal and very small, $\beta_{xz} = \beta_{yz} = 5 \times 10^{-4}$, and the inclusion contains only one micropipe at the corner. (b) The inclusion plastic distortion components are equal and very large, $\beta_{xz} = \beta_{yz} = 0.05$, and the inclusion contains a dislocated elliptic pore which is produced by the coalescence of 306 micropipes and occupies the whole inclusion facet. The arrows show the force directions, and their length is proportional to the force magnitude.

For simplicity, in the following analysis we presume that all micropipes attracted to the inclusion boundary have the same Burgers vectors **b** and the same radii R_0 (Fig. 13). The micropipe radius R_0 is supposed to be related to its Burgers vector magnitude b by the Frank relation (Frank, 1951) $R_0 = Gb^2/(8\pi^2\gamma)$, where G is the shear modulus and γ is the specific surface energy. Also, the pore is assumed to grow in such a way that one of its semiaxes q is constant and equal to the micropipe radius R_0 ($q = R_0$), while the other semiaxis p increases. The volume of the elliptic pore is supposed to be equal to the total volume of the micropipes that merge to form the pore. The free volume conservation equation $\pi pq = N\pi R_0^2$ (where N is the number of micropipes agglomerated into the pore) along with the relation $q = R_0$ gives the following expression for the larger pore semiaxis p: $p = NR_0$.

To analyze the conditions for pore growth, we have calculated the force $\mathbf{F} = F_x\mathbf{e}_x + F_y\mathbf{e}_y$ exerted on a micropipe by the inclusion containing the pore. To do so, we have neglected the short-range effect of the micropipe free surface and considered the micropipe as a screw dislocation with the Burgers vector **b** and coordinates (x_p, y_p) (Fig. 13). The inclusion stress field has been calculated by integrating the stresses of virtual screw dislocations distributed over inclusion facets, with the density determined by the value of the corresponding component of inclusion plastic distortion. To account for the influence of the elliptic pore, we have used the solution for a screw dislocation near an elliptic pore (Zhang & Li, 1991) in the calculation of the stress field of an individual virtual dislocation. The same solution was used to separately account for micropipe attraction to the free surface of the elliptic pore. The calculation scheme used to cast the quantities F_x and F_y is described in (Gutkin et al., 2009b).

As an example, in the following analysis, we consider a 4*H*-SiC inclusion in the 6*H*-SiC matrix. We assume that the inclusion has the square cross-section with the facet dimension of 200 μm and put $\gamma/G = 1.4 \times 10^{-3}$ nm (Si et al., 1997). The magnitude of the micropipe dislocation Burgers vector is chosen to take the values of 4*c*, where $c \approx 1$ nm is the 4*H*-SiC lattice parameter (Goldberg et al., 2001).

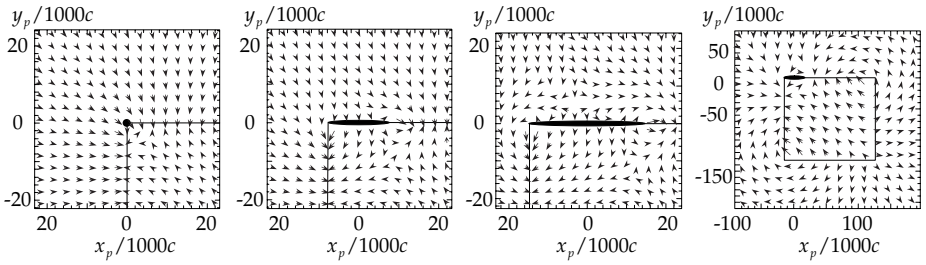

(a) 1 micropipe (b) 35 micropipes (c) 70 micropipes (d) re-scaled (c)

Fig. 15. Vector fields of the force **F** exerted by a 4*H*-SiC inclusion (containing a pore on its boundary) in a 6*H*-SiC matrix on a mobile micropipe with the magnitude 4*c* of the dislocation Burgers vector, for $\beta_{xz} = \beta_{yz} = 5 \times 10^{-3}$. (a) One micropipe lies at the inclusion corner, and another one is attracted to the same place. (b) 35 micropipes merge into the pore, which still attracts new micropipes. (c) 70 micropipes merge into the pore, and the latter starts to repulse new micropipes. (d) Figure (c) in a smaller scale. The arrows show the force directions, and their length is proportional to the force magnitude.

Consider pore growth in the case of equal plastic distortions $\beta_{xz} = \beta_{yz} = \beta$. Figures 14(a) and 14(b) show the final pore configurations when β is very small and very large, respectively. If β is very small (here we take $\beta = 5 \times 10^{-4}$), only one micropipe is attracted to its equilibrium position at the inclusion corner [Fig. 14(a)]. The following micropipes attracted to the inclusion boundary will come to new equilibrium positions at the inclusion boundary far away from the corner. As a result, micropipes do not merge into a larger pore. In contrast, if β is very large (here $\beta = 0.05$), the following micropipes come first to the corner and further to the growing pore. In this case, the pore can occupy the whole inclusion facet, which is illustrated in Fig. 14(b).

The process of pore growth in the intermediate case (here $\beta = 5 \times 10^{-3}$) is shown step by step in Fig. 15. Initially, the first micropipe is attracted to its equilibrium position at the inclusion corner [Fig. 15(a)]. Then new micropipes are attracted to the same equilibrium position and merge, thereby forming a pore. When the pore is not too large, the value of inclusion plastic distortion is sufficient for the pore to attract new micropipes. This case is illustrated in Fig. 15(b), which shows the force vector field (acting on micropipes) around the pore that has absorbed 35 micropipes. However, the situation drastically changes when the pore size becomes large enough [Fig. 15(c)]. Although in this situation a micropipe attraction region still exists near the pore surface, the force on the micropipe is repulsive at some distance from the pore, and the micropipe cannot approach the pore. Under the action of the force field, the micropipe has to round the pore and come to a new equilibrium position at the inclusion boundary far from the pore. The presence of a new equilibrium position for new micropipes is clearly seen in Fig. 15(d), which represents Fig. 15(c) in a smaller scale.

Thus, the analysis of the forces exerted on micropipes by the inclusion and elliptic pore has shown that the pore attracts micropipes until their number reaches a critical value. After that, the micropipes absorbed by the pore produce a repulsion zone for new micropipes, and pore growth stops. The critical pore size is determined by the values of inclusion plastic distortions. At their small values, isolated micropipes form at the inclusion/matrix interface; at medium values micropipes coalesce to form a pore of a certain size; at large values the pore occupies the whole inclusion boundary.

6. Summary

We have briefly reviewed our recent experimental and theoretical studies of collective behavior of micropipes during the bulk SiC growth. The micropipes grow up with the propagation of the crystal growth front and come into reactions with each other as well as with other structural imperfections like foreign polytype inclusions and pores. The reactions between micropipes are either contact-free or contact. A contact-free reaction occurs when one micropipe emits a full-core dislocation, while another micropipe accepts it. We have theoretically described the conditions necessary for such a reaction and provided its indirect experimental evidence. As to contact reactions, we have experimentally documented different transformations and reactions between micropipes in SiC crystal, such as ramification of a dislocated micropipe into two smaller ones, bundling and merging that led to the generation of new micropipes or annihilation of initial ones, interaction of micropipes with foreign polytype inclusions followed by agglomeration and coalescence of micropipes into pores. Theoretical analyses of each configuration have shown that micropipe split happens if the splitting dislocation overcomes the pipe attraction zone and the crystal surface attraction zone. Bundles and twisted dislocation dipoles arise when two micropipes are under strong influence of the stress fields from dense groups of other micropipes. Foreign polytype inclusions attract micropipes due to the action of inclusion stress fields. The micropipe absorption by a pore that has been nucleated at the boundary of inclusion depends on the inclusion distortion. The pore growth stops when the pore absorbs a critical amount of micropipes or occupies the whole inclusion boundary. The general issue is that any kind of the above reactions is quite desired because they always lead to micropipe healing and/or cleaning the corresponding crystal areas from micropipes. Moreover, the contact-free reactions can be treated as a mechanism of thermal stress relaxation, while the micropipe interaction with foreign polytype inclusions and accumulation on their boundaries is a mechanism of misfit stress accommodation.

7. Acknowledgements

This work was supported by the Creative Research Initiatives (Functional X-ray Imaging) of MEST/NRF of Korea. Support of the Russian Foundation of Basic Research (Grant No 10-02-00047-a) is also acknowledged.

8. References

Chen, Y. ; Dudley, M.; Sanchez, E. K.; Macmillan, M. F. (2008). Simulation of grazing-incidence synchrotron white beam X-ray topographic images of micropipes in 4*H*-SiC and determination of their dislocation senses. *J. Electron. Mater.*, Vol. 37, No. 5, 713–720, ISSN: 0361-5235.

Dudley, M.; Huang, X.-R.; Vetter, W. M. (2003) Contribution of x-ray topography and high-resolution diffraction to the study of defects in SiC. *J. Phys. D: Appl. Phys.*, Vol. 36, No. 10A, A30–36, ISSN 0022-3727.

Epelbaum, B. M. & Hofmann, D. (2001). On the mechanisms of micropipe and macrodefect transformation in SiC during liquid phase treatment . *J. Cryst. Growth*, Vol. 225, 1–5, ISSN: 0022-0248.

Frank, F. C. (1951). Capillary equilibria of dislocated crystals. *Acta Crystallogr.*, Vol. 4, 497–501, ISSN: 0108-7673.

Goldberg, A.; Levinstein, M. E.; Rumyantsev, S. L. (2001). In: *Properties of Advanced Semiconductor Materials GaN, AlN, InN, BN, SiC, SiGe*, Levinstein, M. E.; Rumyantsev, S. L.; Shur, M. S. (Eds.), 93, Wiley, New York.

Gutkin, M. Yu.; Sheinerman, A. G.; Argunova, T. S.; Je, J.-H.; Kang, H.-S., Hwu, Y.; Tsai, W.-L. (2002). Ramification of micropipes in SiC crystals. *J. Appl. Phys.*, Vol. 92, No. 2, 889–894, ISSN 0021-8979.

Gutkin, M. Yu. & Sheinerman, A. G. (2002). Elastic Interaction of Micropipes in Crystals. *Physica Status Solidi B*, Vol. 231, No. 2, 356–372, ISSN: 1521-3951.

Gutkin, M. Yu.; Sheinerman, A. G.; Argunova, T. S.; Mokhov, E. N.; Je, J.-H.; Hwu, Y.; Tsai, W.-L.; Margaritondo, G. (2003). Micropipe evolution in silicon carbide. *Appl. Phys. Lett.*, Vol. 83, No. 11, 2157–2159, ISSN 0003-6951.

Gutkin, M. Yu.; Sheinerman, A. G.; Argunova, T. S.; Mokhov, E. N.; Je, J.-H.; Hwu, Y.; Tsai, W.-L.; Margaritondo, G. (2003). Synchrotron radiographic study and computer simulation of reactions between micropipes in silicon carbide. *J. Appl. Phys.*, Vol. 94, No. 11, 7076–7082, ISSN 0021-8979.

Gutkin, M. Yu. & Sheinerman, A. G. (2004). Split and sealing of dislocated pipes at the front of a growing crystal. *Physica Status Solidi B*, Vol. 241, No. 8, 1810–1826, ISSN: 1521-3951.

Gutkin, M. Yu.; Sheinerman, A. G.; Argunova, T. S.; Yi, J.-M.; Kim, M.-U.; Je, J.-H.; Nagalyuk, S. S.; Mokhov, E. N.; Margaritondo, G.; Hwu, Y. (2006). Interaction of micropipes with foreign polytype inclusions in SiC. *J. Appl. Phys.*, Vol. 100, 093518 (10 pp.), ISSN 0021-8979.

Gutkin, M. Yu.; Sheinerman, A. G.; Smirnov, M. A.; Kohn, V. G.; Argunova, T. S.; Je, J.-H.; Jung, J.-W. (2008). Correlated reduction in micropipe cross sections in SiC growth. *Appl. Phys. Lett.*, Vol. 93, 151905 (3 pp.), ISSN 0003-6951.

Gutkin, M. Yu.; Sheinerman, A. G.; Argunova, T. S. (2009). Micropipes in silicon carbide crystals. *Phys. Stat. Sol. C*, Vol. 6, No. 8, 1942–1947, ISSN: 1610-1642.

Gutkin, M. Yu.; Sheinerman, A. G.; Smirnov, M. A.; Argunova, T. S.; Je, J.-H.; Nagalyuk, S. S.; Mokhov, E. N. (2009). Micropipe absorption mechanism of pore growth at foreign polytype boundaries in SiC crystals. *J. Appl. Phys.*, Vol. 106, 123515 (7 pp.), ISSN 0021-8979.

Gutkin, M. Yu.; Sheinerman, A. G.; Smirnov, M. A. (2009). Elastic behavior of screw dislocations in porous solids. *Mech. Mater.*, Vol. 41, No. 8, 905–918, ISSN: 0167-6636.

Hirth, J. P. & Lothe, J. (1982). Theory of Dislocations, Wiley, New York.

Huang, X. R.; Dudley, M.; Vetter, W. M.; Huang, W.; Wang, S. (1999). Direct evidence of micropipe-related pure superscrew dislocations in SiC. *Appl. Phys. Lett.*, Vol. 74, No. 3; 353–355, ISSN 0003-6951.

Kamata, I.; Tsuchida, H.; Jikimoto, T.; Izumi, K. (2000). Structural transformations of screw dislocations via thick 4*H*-SiC epitaxial overgrowth. *Jpn. J. Appl. Phys.*, Vol. 39, No. 12A, 6496–6500, ISSN 0021-4922.

Kamata, I.; Nagano, M.; Tsuchida, H.; Chen, Y.; Dudley, M. (2009). Investigation of character and spatial distribution of threading edge dislocations in 4*H*-SiC epilayers by high-resolution topography. *J. Cryst. Growth*, Vol. 311, 1416–1422, ISSN: 0022-0248.

Kohn, V. G.; Argunova, T. S.; Je, J.-H. (2007). Study of micropipe structure in SiC by x-ray phase contrast imaging. *Appl. Phys. Lett.*, Vol. 91, 171901 (3 pp.), ISSN 0003-6951.

Ma, R.-H.; Zhang, H.; Dudley M.; Prasad, V. (2003). Thermal system design and dislocation reduction for growth of wide band gap crystals: : application to SiC growth. *J. Cryst. Growth*, Vol. 258, No. 3–4, 318–330. ISSN: 0022-0248.

Ma, X. (2006). Superscrew dislocations in silicon carbide: Dissociation, aggregation, and formation. *J. Appl. Phys.*, Vol. 99, 063513 (6 pp.), ISSN 0021-8979.

Müller, St. G.; Glass, R. C.; Hobgood, H. McD.; Tsvetkov, V. F.; Brady, M.; Henshall, D.; Jenny, J. R.; Malta, D.; Carter Jr., C. H. (2000). The status of SiC bulk growth from an industrial point of view. *J. Cryst. Growth*, Vol. 211, No. 1–4, 325–332, ISSN: 0022-0248.

Müller, St. G.; Brady, M. F.; Burk, A. A.; Hobgood, H. McD; Jenny, J. R.; Leonard, R. T.; Malta, D. P.; Powell, A. R.; Sumakeris, J. J.; Tsvetkov, V. F.; Carter Jr., C. H. (2006). Large area SiC substrates and epitaxial layers for high power semiconductor devices - An industrial perspective. *Superlattices Microst.*, Vol. 40, 195–200, ISSN: 0749-6036.

Nakamura, D.; Gunjishima, I.; Yamaguchi, S.; Ito, T.; Okamoto, A.; Kondo, H.; Onda, S.; Takatori K. (2004). Ultrahigh-quality silicon carbide single crystals. *Let. Nature*, Vol. 430, 1009–1012, ISSN: 0028-0836.

Nakamura, D.; Yamaguchi, S.; Gunjishima, I.; Hirose, Y.; Kimoto T. (2007). Topographic study of dislocation structure in hexagonal SiC single crystals with low dislocation density. *J. Cryst. Growth*, Vol. 304, 57–63, ISSN: 0022-0248.

Nakamura, D.; Yamaguchi, S.; Hirose, Y.; Tani, T.; Takatori, K.; Kajiwara, K.; Kimoto T. (2008). Direct determination of Burgers vector sense and magnitude of elementary dislocations by synchrotron white x-ray topography. *J. Appl. Phys.*, Vol. 103, 013510 (7 pp.), ISSN 0021-8979.

Ohtani, N.; Katsuno, M.; Tsuge, H.; Fujimoto, T.; Nakabayashi, M.; Yashiro, H.; Sawamura, M.; Aigo, T.; Hoshino T. (2006). Propagation behavior of threading dislocations during physical vapor transport growth of silicon carbide (SiC) single crystals. *J. Cryst. Growth*, Vol. 286, 55–60, ISSN: 0022-0248.

Pirouz, P. (1998). On micropipes and nanopipes in SiC and GaN. *Philos. Mag. A*, Vol. 78, No. 3, 727–736, ISSN: 1478-6435.

Saparin, G. V.; Obyden, S. K.; Ivannikov, P. V.; Shishkin, E. B.; Mokhov, E. N.; Roenkov, A. D.; Hofmann, D. H. (1997). Three-Dimensional Studies of SiC Polytype Transformations. *Scanning*, Vol. 19, 269–274, ISSN: 1932-8745.

Si, W.; Dudley, M.; Glass, R.; Tsvetkov, V.; Carter Jr., C. (1997). Hollow-core screw dislocations in 6*H*-SiC single crystals: A test of Frank's theory. *J. Electron. Maters.*, Vol. 26, No. 3, 128–133, ISSN: 0361-5235.

Thölén, A. R. (1970). The stress field of a pile-up of screw dislocations at a cylindrical inclusion. *Acta Metall.*, Vol. 18, No. 4, 445–455, ISSN: 1359-6454

Tsuchida, H.; Kamata, I.; Nagano M. (2007). Investigation of defect formation in 4*H*-SiC epitaxial growth by X-ray topography and defect selective etching. *J. Cryst. Growth*, Vol. 306, 254–261, ISSN: 0022-0248.

Vodakov, Yu. A.; Roenkov, A. D.; Ramm, M. G.; Mokhov, E. N.; Makarov, Yu. N. (1997). Use of Ta-container for sublimation growth and doping of SiC bulk crystals and epitaxial layers. *Phys. Status Solidi B*, Vol. 202, 177–200, ISSN: 1521-3951.

Wang, Y.; Ali, G. N.; Mikhov, M. K.; Vaidyanathan, V.; Skromme, B. J.; Raghothamachar, B.; Dudley, M. (2005). Correlation between morphological defects, electron beam-induced current imaging, and the electrical properties of 4*H*-SiC Schottky diodes. *J. Appl. Phys.*, Vol. 97, 013540 (10 pp.), ISSN 0021-8979.

Wierzchowski, W.; Wieteska, K.; Balcer, T.; Malinowska, A.; Graeff, W.; Hofman, W. (2007). Observation of individual dislocations in 6*H* and 4*H*-SiC by means of back-reflection methods of X-ray diffraction topography. *Cryst. Res. Technol.*, Vol. 42, No. 12, 1359–1363, ISSN: 0232-1300.

Yakimova, R.; Vouroutzis, N.; Syväjärvi, M.; Stoemenos, J. (2005). Morphological features related to micropipe closing in 4*H*-SiC. *J. Appl. Phys.*, Vol. 98, 034905 (6 pp.), ISSN 0021-8979.

Zhang, T-Y. & Li, J. C. M. (1991). Image forces and shielding effects of a screw dislocation near a finite-length crack. *Mater. Sci. and Eng. A*, Vol. 142, No. 1, 35-39, ISSN: 0921-5093.